Monthly Notices of the ROYAL ASTRONOMICAL SOCIETY

MNRAS **498,** 495–506 (2020) doi:10.1093/mnras/staa2286
Advance Access publication 2020 August 5

Binary black holes in young star clusters: the impact of metallicity

Ugo N. Di Carlo [1,2,3★] Michela Mapelli [2,3,4] Nicola Giacobbo [2,3,4] Mario Spera [2,4,5,6] Yann Bouffanais,[2,4] Sara Rastello [2,4] Filippo Santoliquido,[2,4] Mario Pasquato,[2,3] Alessandro Ballone [2,4] Alessandro A. Trani,[7,8] Stefano Torniamenti[2,4] and Francesco Haardt[1]

[1]*Dipartimento di Scienza e Alta Tecnologia, University of Insubria, Via Valleggio 11, I-22100 Como, Italy*
[2]*INFN, Sezione di Padova, Via Marzolo 8, I-35131 Padova, Italy*
[3]*INAF – Osservatorio Astronomico di Padova, Vicolo dell'Osservatorio 5, I-35122 Padova, Italy*
[4]*Dipartimento di Fisica e Astronomia 'G. Galilei', University of Padova, Vicolo dell'Osservatorio 3, I-35122 Padova, Italy*
[5]*Center for Interdisciplinary Exploration and Research in Astrophysics (CIERA), Evanston, IL 60208, USA*
[6]*Department of Physics and Astronomy, Northwestern University, Evanston, IL 60208, USA*
[7]*Department of Astronomy, Graduate School of Science, The University of Tokyo, 7-3-1 Hongo, Bunkyo-ku, Tokyo 113-0033, Japan*
[8]*Department of Earth Science and Astronomy, College of Arts and Sciences, The University of Tokyo, 3-8-1 Komaba, Meguro-ku, Tokyo 153-8902, Japan*

Accepted 2020 July 27. Received 2020 July 26; in original form 2020 April 22

ABSTRACT

Young star clusters are the most common birthplace of massive stars and are dynamically active environments. Here, we study the formation of black holes (BHs) and binary black holes (BBHs) in young star clusters, by means of 6000 *N*-body simulations coupled with binary population synthesis. We probe three different stellar metallicities ($Z = 0.02$, 0.002, and 0.0002) and two initial-density regimes (density at the half-mass radius $\rho_{\rm h} \geq 3.4 \times 10^4$ and $\geq 1.5 \times 10^2$ $M_\odot$ pc^{-3} in dense and loose star clusters, respectively). Metal-poor clusters tend to form more massive BHs than metal-rich ones. We find ∼6, ∼2, and <1 per cent of BHs with mass $m_{\rm BH} > 60$ $M_\odot$ at $Z = 0.0002$, 0.002, and 0.02, respectively. In metal-poor clusters, we form intermediate-mass BHs with mass up to ∼320 $M_\odot$. BBH mergers born via dynamical exchanges (exchanged BBHs) can be more massive than BBH mergers formed from binary evolution: the former (latter) reach total mass up to ∼140 $M_\odot$ (∼80 $M_\odot$). The most massive BBH merger in our simulations has primary mass ∼88 $M_\odot$, inside the pair-instability mass gap, and a mass ratio of ∼0.5. Only BBHs born in young star clusters from metal-poor progenitors can match the masses of GW 170729, the most massive event in first and second observing run (O1 and O2), and those of GW 190412, the first unequal-mass merger. We estimate a local BBH merger rate density ∼110 and ∼55 Gpc^{-3} yr^{-1}, if we assume that all stars form in loose and dense star clusters, respectively.

Key words: black hole physics – gravitational waves – methods: numerical – binaries: general – stars: kinematics and dynamics – galaxies: star clusters: general.

1 INTRODUCTION

About 4 yr ago, the LIGO–Virgo Collaboration (LVC; Aasi et al. 2015; Acernese et al. 2015) reported the very first direct detection of gravitational waves, GW 150914, interpreted as the merger of two massive stellar black holes (BHs; Abbott et al. 2016b,d). After GW 150914, nine additional binary black holes (BBHs) and one binary neutron star (BNS) were observed by the LVC during the first and second observing run (hereafter O1 and O2; Abbott et al. 2016a, 2019a,b). The third observing run of LIGO and Virgo has recently been completed and has already led to one additional BNS (GW 190425; Abbott et al. 2020b), the first unequal-mass BBH merger (GW 190412; Abbott et al. 2020a), and tens of public alerts.[1]

Understanding the formation channels of BBHs is one of the most urgent astrophysical questions raised by LVC observations. Several authors suggest that about a hundred of detections are sufficient to say something on the formation channels of BBHs, thanks to their distinctive signatures (e.g. Fishbach, Holz & Farr 2017; Gerosa & Berti 2017; Stevenson, Berry & Mandel 2017; Gerosa et al. 2018; Bouffanais et al. 2019).

Isolated binary evolution, either via common envelope (e.g. Tutukov & Yungelson 1973; Bethe & Brown 1998; Portegies Zwart & Yungelson 1998; Belczynski, Kalogera & Bulik 2002; Voss & Tauris 2003; Podsiadlowski et al. 2004; Belczynski et al. 2008, 2016; Dominik et al. 2012, 2013; Mennekens & Vanbeveren 2014; Mapelli et al. 2017, 2019; Giacobbo & Mapelli 2018; Giacobbo, Mapelli & Spera 2018; Kruckow et al. 2018; Mapelli & Giacobbo 2018; Neijssel et al. 2019; Spera et al. 2019; Tang et al. 2020) or via chemically homogeneous scenarios (de Mink & Mandel 2016; Mandel & de Mink 2016; Marchant et al. 2016), predicts the formation of BBHs with primary mass up to ∼40–65 $M_\odot$ (see e.g. Mapelli et al. 2020 and references therein), with a strong preference for equal-mass systems, mostly aligned spins and zero eccentricity in the LVC band.

In contrast, dynamical formation in star clusters might lead to even larger primary masses (e.g. McKernan et al. 2012, 2018; Antonini & Rasio 2016; Mapelli 2016; Gerosa & Berti 2017; Stone, Metzger & Haiman 2017; Arca Sedda & Benacquista 2019; Di Carlo et al. 2019, 2020; Rodriguez et al. 2019; Yang et al. 2019; Arca Sedda et al.

★ E-mail: ugo_dc@hotmail.it
[1]https://gracedb.ligo.org/

2020), mass ratios ranging from $q \sim 0.1$ to ~ 1 (e.g. Di Carlo et al. 2019), isotropic spin distribution, and, in some rare but not negligible cases, non-zero eccentricity in the LVC band (e.g. Rodriguez et al. 2018; Samsing 2018; Samsing & D'Orazio 2018; Samsing, Askar & Giersz 2018; Zevin et al. 2019).

The zoology of star clusters found in the Universe is rich and includes systems that are extremely different from each other (both in terms of mass and lifetime), but share a similar dynamical evolution: almost all star clusters are collisional systems, i.e. stellar systems in which the two-body relaxation time-scale is shorter than their lifetime (e.g. Spitzer 1987). Hence, close encounters between single and binary (or multiple) stars drive the evolution of star clusters and have a crucial impact on the formation of binary compact objects.

The dynamical evolution of BBHs in nuclear star clusters (e.g. Miller & Lauburg 2009; O'Leary, Kocsis & Loeb 2009; McKernan et al. 2012, 2018; VanLandingham et al. 2016; Stone et al. 2017; Arca-Sedda & Gualandris 2018; Hoang et al. 2018; Antonini, Gieles & Gualandris 2019) and globular clusters (e.g. Sigurdsson & Hernquist 1993; Sigurdsson & Phinney 1995; Portegies Zwart & McMillan 2000; O'Leary et al. 2006; Sadowski et al. 2008; Downing et al. 2010, 2011; Tanikawa 2013; Rodriguez et al. 2015, 2018; Antonini & Rasio 2016; Hurley et al. 2016; O'Leary, Meiron & Kocsis 2016; Rodriguez, Chatterjee & Rasio 2016; Askar et al. 2017; Zevin et al. 2017; Askar, Arca Sedda & Giersz 2018; Antonini et al. 2019; Choksi et al. 2019) has been extensively investigated. These are the most massive, long-lived, and predominantly old stellar systems; hence their relatively high escape velocity allows a fraction of the merger remnants to stay in the cluster, leading to a population of hierarchical mergers (Miller & Hamilton 2002; Arca Sedda & Benacquista 2019; Gerosa & Berti 2019; Rodriguez et al. 2019).

Young star clusters (YSCs) and open clusters are generally smaller and shorter lived than globular clusters (Portegies Zwart, McMillan & Gieles 2010). None the less, they are site of strong dynamical interactions and they are the nursery of massive stars in the Universe: the vast majority of massive stars, which are the progenitors of compact objects, form in YSCs (e.g. Lada & Lada 2003; Portegies Zwart et al. 2010). Hence, the majority of BHs have likely spent the first part of their life in star clusters, undergoing dynamical encounters. Several studies demonstrate that dynamics has a major role in the formation of BH binaries in YSCs (Portegies Zwart & McMillan 2002; Banerjee, Baumgardt & Kroupa 2010; Mapelli et al. 2013; Goswami, Kiel & Rasio 2014; Mapelli & Zampieri 2014; Ziosi et al. 2014; Mapelli 2016; Banerjee 2017, 2018; Fujii, Tanikawa & Makino 2017; Di Carlo et al. 2019; Kumamoto, Fujii & Tanikawa 2019, 2020; Rastello et al. 2019).

In particular, Di Carlo et al. (2019) showed that about half of BBHs born in YSCs form via dynamical exchanges at metallicity $Z = 0.002$. BBHs formed in YSCs are significantly more massive than BBHs formed from isolated binary evolution and tend to have smaller mass ratios. About ~ 2 per cent of all BBH mergers originating from YSCs have primary mass $\gtrsim 60$ M$_\odot$, falling inside the pair-instability mass gap (e.g. Spera & Mapelli 2017; Woosley 2017; Farmer et al. 2019; Marchant et al. 2019; Stevenson et al. 2019; Di Carlo et al. 2020; Mapelli et al. 2020; Renzo et al. 2020). The sample presented in Di Carlo et al. (2019) is the largest simulation set of YSCs used to study BBHs, but is limited to one metallicity $Z = 0.002$. Since metallicity has a crucial impact on the mass of BHs (Mapelli, Colpi & Zampieri 2009; Zampieri & Roberts 2009; Belczynski et al. 2010; Mapelli et al. 2010; Spera, Mapelli & Bressan 2015), it is essential to study the evolution of BBHs in star clusters with different metallicity. In this paper, we present the result of a new set of simulations where we consider three different metallicities ($Z = 0.02$, 0.002, and 0.0002) and two initial-density regimes (density at the half-mass radius $\rho_{\rm h} \geq 3.4 \times 10^4$ and $\geq 1.5 \times 10^2$ M$_\odot$ pc^{-3} in dense and loose star clusters, respectively).

2 METHODS

The simulations discussed in this paper were done using the same code and methodology as described in Di Carlo et al. (2019). In particular, we use the direct summation *N*-body code NBODY6++GPU (Wang et al. 2015) coupled with the population-synthesis code MOBSE (Mapelli et al. 2017; Giacobbo & Mapelli 2018; Giacobbo et al. 2018).

2.1 Direct *N*-body

NBODY6++GPU is the GPU parallel version of NBODY6 (Aarseth 2003). It implements a fourth-order Hermite integrator, individual block time steps (Makino & Aarseth 1992), and Kustaanheimo–Stiefel (KS) regularization of close encounters and few-body subsystems (Stiefel 1965; Mikkola & Aarseth 1993).

A neighbour scheme (Nitadori & Aarseth 2012) is used to compute the force contributions at short time intervals (*irregular* force/time steps), while at longer time intervals (*regular* force/time steps) all the members in the system contribute to the force evaluation. The irregular forces are evaluated using CPUs, while the regular forces are computed on GPUs using the CUDA architecture. This version of NBODY6++GPU does not include post-Newtonian terms.

2.2 Population synthesis

MOBSE (Mapelli et al. 2017; Giacobbo & Mapelli 2018, 2019; Giacobbo et al. 2018; Mapelli & Giacobbo 2018) is a customized and upgraded version of BSE (Hurley, Pols & Tout 2000; Hurley, Tout & Pols 2002) that includes up-to-date prescriptions for massive star winds, for core-collapse supernova (SN) explosions, and for pair-instability and pulsational-pair-instability SNe. It has been integrated with NBODY6++GPU by taking advantage of the pre-existing interface between the *N*-body code and BSE.

Stellar winds are implemented assuming that the mass loss of massive hot stars (O- and B-type stars, Wolf–Rayet stars, and luminous blue variable stars) depends on metallicity as $\dot{M} \propto Z^{\beta}$, where β is defined as in Giacobbo et al. (2018):

$$\beta = \begin{cases} 0.85 & \text{if} \quad \Gamma_{\rm e} < 2/3, \\ 2.45 - 2.4\Gamma_{\rm e} & \text{if} \quad 2/3 \leq \Gamma_{\rm e} < 1, \\ 0.05 & \text{if} \quad \Gamma_{\rm e} \geq 1. \end{cases} \tag{1}$$

Here $\Gamma_{\rm e}$ is the Eddington factor (see e.g. Gräfener & Hamann 2008; Chen et al. 2015).

The outcome of core-collapse SNe is highly uncertain and none of the prescriptions available in the literature are completely satisfactory (e.g. Burrows et al. 2018; Mapelli et al. 2020). Hence, our prescriptions should be regarded as reasonable 'toy models'. In this paper, we adopt the rapid core-collapse SN model described in Fryer et al. (2012). In this formalism, the mass of the compact object is $m_{\rm rem} = m_{\rm proto} + m_{\rm fb}$, where $m_{\rm proto} = 1$ M$_\odot$ is the mass of the protocompact object and $m_{\rm fb}$ is the mass accreted by fallback. Note that this is different from Di Carlo et al. (2019), where we adopted the delayed model from Fryer et al. (2012).

When the helium core of a star becomes $64 \leq m_{\rm He}/{\rm M}_\odot \leq 135$, the star is completely destroyed by pair instability. If the helium core reaches a size $32 \leq m_{\rm He}/{\rm M}_\odot < 64$, pulsational pair instability is expected to take place (Woosley 2017) and the final mass of the compact

Table 1. Initial conditions.

Set	Z	N_{SC}	M_{SC} ($M_\odot$)	r_h (pc)
YSC	0.02, 0.002, 0.0002	6000	10^3–3×10^4	1.5, 0.1 $(M_{SC}/M_\odot)^{0.13}$
A	0.02, 0.002, 0.0002	3000	10^3–3×10^4	0.1 $(M_{SC}/M_\odot)^{0.13}$
B	0.02, 0.002, 0.0002	3000	10^3–3×10^4	1.5
IB	0.02, 0.002, 0.0002	3×10^7	–	–
A02	0.02	1000	10^3–3×10^4	0.1 $(M_{SC}/M_\odot)^{0.13}$
A002	0.002	1000	10^3–3×10^4	0.1 $(M_{SC}/M_\odot)^{0.13}$
A0002	0.0002	1000	10^3–3×10^4	0.1 $(M_{SC}/M_\odot)^{0.13}$
B02	0.02	1000	10^3–3×10^4	1.5
B002	0.002	1000	10^3–3×10^4	1.5
B0002	0.0002	1000	10^3–3×10^4	1.5
IB02	0.02	10^7	–	–
IB002	0.002	10^7	–	–
IB0002	0.0002	10^7	–	–

Note. Column 1: name of the simulation set; YSC stands for all dynamical simulations (set A and set B) considered together, while IB stands for isolated binaries. Column 2: stellar metallicity (Z). Column 3: number of runs (N_{SC}). Column 4: YSC mass (M_{SC}). Column 5: initial half-mass radius (r_h).

object is estimated as $m_{rem} = \alpha_P\, m_{no\,PPI}$, where $m_{no\,PPI}$ is the mass of the compact object we would have obtained if we had not included pulsational pair instability in our analysis and α_P is a fitting parameter (Spera & Mapelli 2017; Mapelli et al. 2020). Finally, electron-capture SNe are implemented as described in Giacobbo & Mapelli (2019).

Natal kicks are randomly drawn from a Maxwellian velocity distribution. A one-dimensional root mean square velocity $\sigma = 15$ km s^{-1} is adopted for core-collapse SNe and for electron-capture SNe (Giacobbo & Mapelli 2019). Kick velocities of BHs are reduced by the amount of fallback as $V_{KICK} = (1 - f_{fb})\, V$, where f_{fb} is the fallback parameter described in Fryer et al. (2012) and V is the velocity drawn from the Maxwellian distribution.[2]

Binary evolution processes (tides, mass transfer, common envelope, and gravitational wave orbital decay) are implemented as in Hurley et al. (2002). In this work, we assume $\alpha = 5$ (it was $\alpha = 3$ in Di Carlo et al. 2019), while λ is derived by MOBSE as described in Claeys et al. (2014).

Consistently with Di Carlo et al. (2019), when two stars merge, the amount of mass loss is decided by MOBSE, which adopts the same prescriptions as BSE, but if a star merges with a BH or a neutron star, MOBSE assumes that the entire mass of the star is immediately lost by the system and the compact object does not accrete it. This assumption by MOBSE is very conservative, because it is unlikely that the compact object can accrete a substantial fraction of the stellar mass, but it is hard to quantify the actual mass accretion.

2.3 Initial conditions

We have simulated 6000 YSCs considering three different metallicities ($Z = 0.02$, 0.002, and 0.0002) and two definitions for the initial half-mass radius r_h (Table 1). Simulations of set A (3000 simulations, 1000 for each considered metallicity) were performed choosing r_h according to the Marks–Kroupa relation (Marks et al. 2012), which relates the total mass M_{SC} of a star cluster at birth with its initial half mass radius r_h:

$$r_h = 0.10^{+0.07}_{-0.04}\ \mathrm{pc} \left(\frac{M_{SC}}{M_\odot}\right)^{0.13\pm0.04}. \quad (2)$$

Simulations of set B (3000 simulations, 1000 for each considered metallicity) assume $r_h = 1.5$ pc. The initial densities of the YSCs at the half-mass radius are $\rho_h = 500\,(M_{SC}/M_\odot)^{0.61}\ M_\odot\ \mathrm{pc}^{-3}$ and $\rho_h = 4/27\,(M_{SC}/M_\odot)\ M_\odot\ \mathrm{pc}^{-3}$ for set A and B, respectively. We also refer to set A/set B star clusters as dense/loose ones.

As already discussed in Di Carlo et al. (2019), we model YSCs with fractal initial conditions, because this mimics the initial clumpiness and asymmetry of embedded star clusters (Cartwright & Whitworth 2004; Goodwin & Whitworth 2004; Gutermuth et al. 2005; Ballone et al. 2020). We adopt a fractal dimension $D = 1.6$ and generate the initial conditions with MCLUSTER (Küpper et al. 2011). In Di Carlo et al. (2019), we have shown that larger values of the fractal dimension ($D \leq 2.3$) do not significantly affect the statistics of BBHs.

The total mass M_{SC} of each star cluster (ranging from 1000 to 30 000 $M_\odot$) is drawn from a distribution $\mathrm{d}N/\mathrm{d}M_{SC} \propto M_{SC}^{-2}$, as the embedded star cluster mass function described in Lada & Lada (2003). Thus, the mass distribution of our simulated star clusters mimics the mass distribution of star clusters in Milky Way-like galaxies. The star clusters are initialized so that the virial ratio $\alpha_{vir} = T/|V| = 0.5$, where T and V are the total kinetic and potential energy of the YSC, respectively.

The stars in the simulated star clusters follow a Kroupa (2001) initial mass function, with minimum mass 0.1 $M_\odot$ and maximum mass 150 $M_\odot$. We assume an initial binary fraction $f_{bin} = 0.4$, meaning that 40 per cent of the stars are members of binary systems. The orbital periods, eccentricities, and mass ratios of binaries with primary more massive than 5 $M_\odot$ are drawn from Sana et al. (2012) distributions, as already described in Di Carlo et al. (2019). Stars with a mass larger than 5 $M_\odot$, starting from the most massive, are paired with the star that better matches the mass ratio drawn from the distribution. Stars under 5 $M_\odot$ are randomly paired until the required binary fraction is reached. This procedure results in a mass-dependent initial binary fraction that is larger for more massive binaries, consistent with the multiplicity properties of O/B-type stars (e.g. Sana et al. 2012; Moe & Di Stefano 2017), as shown in Fig. 1.

The force integration includes a solar neighbourhood-like static external tidal field (Wang et al. 2016). Each star cluster is evolved

[2]This kick model was chosen because it leads to a BNS merger rate in agreement with the range inferred from the LVC (Baibhav et al. 2019), but is in tension with the proper motions of young Galactic pulsars (Hobbs et al. 2005). In a recent work (Giacobbo & Mapelli 2020), we have revised our kick prescriptions and we have shown that the value of σ adopted in this work has negligible effect on the properties and on the merger rate of BBHs (because V_{KICK} is dominated by fallback).

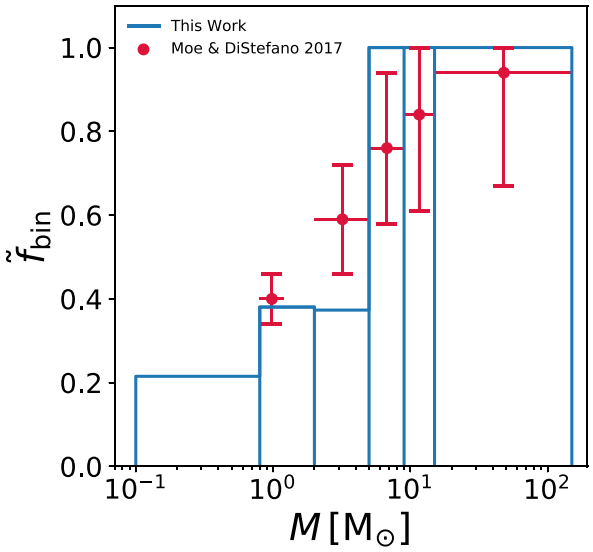

Figure 1. Initial binary fraction $\widetilde{f}_{\rm bin}$ as a function of stellar mass. $\widetilde{f}_{\rm bin}$ is defined as $N_{\rm bin}/(N_{\rm bin}+N_{\rm sin})$, where $N_{\rm bin}$ is the total number of binaries and $N_{\rm sin}$ is the total number of single stars in the YSC at the beginning of the simulation. The blue line represents the binary fraction for one of our simulated star clusters, while the red circles come from the observational results (Moe & Di Stefano 2017) and represent the fraction of stars with at least one companion.

until its dissolution or for a maximum time $t = 100$ Myr. The most massive star clusters in our sample are not completely disrupted at $t = 100$ Myr, but our static tidal field model tends to overestimate the lifetime of star clusters, because it does not account for massive perturbers (e.g. molecular clouds), which can accelerate star cluster disruption (Gieles et al. 2006). Hence, our choice is quite conservative. When the *N*-body simulation stops, we extract all the BBHs and we evolve their semimajor axis and eccentricity using the time-scale formula presented in Peters (1964), which describes the evolution of the orbit due to gravitational wave emission. We classify as merging BBHs all BBHs that merge within a Hubble time ($t_{\rm H} = 14$ Gyr) by gravitational wave decay.

For comparison, we have also run a set of isolated binary simulations with the stand-alone version of MOBSE. In particular, we simulated 10^7 isolated binaries for each considered metallicity ($Z = 0.02$, 0.002, and 0.0002). Primary masses of the isolated binaries are drawn from a Kroupa (Kroupa 2001) mass function between 5 and 150 $M_\odot$. Orbital periods and eccentricities are randomly drawn from the same distribution as the dynamical simulations, but for one difference: the maximum orbital period is $\log(P_{\rm max}/{\rm d}) = 5.5$ and 6.7 in the isolated binaries and in the dynamical simulations, respectively. We checked that this difference has a negligible impact on our results. A summary of the initial conditions of the performed simulations is reported in Table 1.

3 RESULTS

3.1 BH mass distribution

Fig. 2 shows the mass distribution of all simulated BHs. The overall mass range of BHs, considering both single and binary BHs, spans from 5 $M_\odot$ (the minimum BH mass according to the rapid model by Fryer et al. 2012) to 320 $M_\odot$.

The maximum BH mass and the slope of the BH mass function depend on metallicity: BHs born from metal-rich stars ($Z = 0.02$) tend to be less massive than BHs born from metal-poor stars ($Z = 0.0002$–0.002).

In the case of single stars and isolated binaries, MOBSE predicts a maximum BH mass of $\sim$65 $M_\odot$ (see fig. 4 in Giacobbo et al. 2018), while in our dynamical simulations we find BHs with mass up to $\sim$320 $M_\odot$. This difference is a result of multiple stellar mergers in YSCs, which build-up a significantly more massive BH population in star clusters than in the field. This produces a non-negligible population of BHs with mass in the pair-instability gap, between $\sim$60 and $\sim$120 $M_\odot$: $\sim$5.0, 1.5, and 0.2 per cent ($\sim$5.7, $\sim$2.2, and $\sim$0.01 per cent) of the simulated BHs have mass in the pair-instability gap in our set A (set B) at $Z = 0.0002$, 0.002, and 0.02, respectively.

Intermediate-mass BHs (IMBHs), defined as BHs with $m_{\rm BH} \geq 100$ $M_\odot$, are $\sim$0.5, $\sim$0.3, and $\sim$0.03 per cent ($\sim$0.4, $\sim$0.1, and $\sim$0.02 per cent) of all our BHs in set A (set B) at $Z = 0.0002$, 0.002, and 0.02, respectively. They form through (multiple) stellar mergers, whose probability is enhanced by the short dynamical friction time-scale in our clusters ($t_{\rm df} \lesssim 1$ Myr for a star with zero-age main-sequence mass $m_{\rm ZAMS} \gtrsim 20$ $M_\odot$): the most massive stars and binary stars sink to the core of the cluster before they become BHs; once in the core, they interact with each other triggering the mechanism known as runaway collision (e.g. Portegies Zwart & McMillan 2002; Portegies Zwart et al. 2004; Giersz et al. 2015; Mapelli 2016).

The mass distribution of BHs in dense clusters (set A) and loose clusters (set B) is similar. The main difference is the percentage of BBHs that merge within a Hubble time (hereafter, merging BBHs), especially at low metallicity: these are $\sim$17.1, $\sim$5.7, and $\sim$1.7 per cent ($\sim$3.9, $\sim$2.0, and $\sim$1.8 per cent) in set A (set B) for a progenitor metallicity $Z = 0.0002$, 0.002, and 0.02, respectively. Hence, star cluster density plays an important role in shrinking the orbit of BBHs. From these numbers, it is also apparent that BBH mergers are more common at low metallicity.

3.2 Properties of merging BBHs

Here, we focus on merging BBHs, i.e. BBHs that reach coalescence within a Hubble time. We call dynamical BBHs and isolated BBHs those merging BBHs that form in YSCs and in isolated binaries, respectively. We further divide dynamical BBHs into exchanged BBHs (i.e. dynamical BBHs that form from dynamical exchanges) and original BBHs (i.e. dynamical BBHs that form from binary stars that were already present in the initial conditions).[3]

Table 2 shows the percentage of original and exchanged BBHs for each set. About 78 per cent of all BBHs are exchanged, but only $\sim$43 per cent of the merging BBHs are exchanged. This indicates that a large fraction of exchanged BBHs are loose binaries and cannot harden fast enough to merge within a Hubble time. The percentage of exchanged BBHs in set A is higher than that of set B: binaries in dense star clusters undergo more exchanges than in loose star clusters.

The fraction of exchanged BBHs increase with metallicity in set A, while it is almost constant with metallicity in set B. For example, the

[3]In papers about star cluster dynamics, original BBHs are usually referred to as 'primordial BBHs' or 'BBHs born from primordial binaries', because the binary stars that were already present in the initial conditions are usually called 'primordial binaries'. Here, we name them original BBHs to avoid confusion with primordial BHs that might form from gravitational instabilities in the early Universe (e.g. Carr & Hawking 1974; Carr, Kühnel & Sandstad 2016).

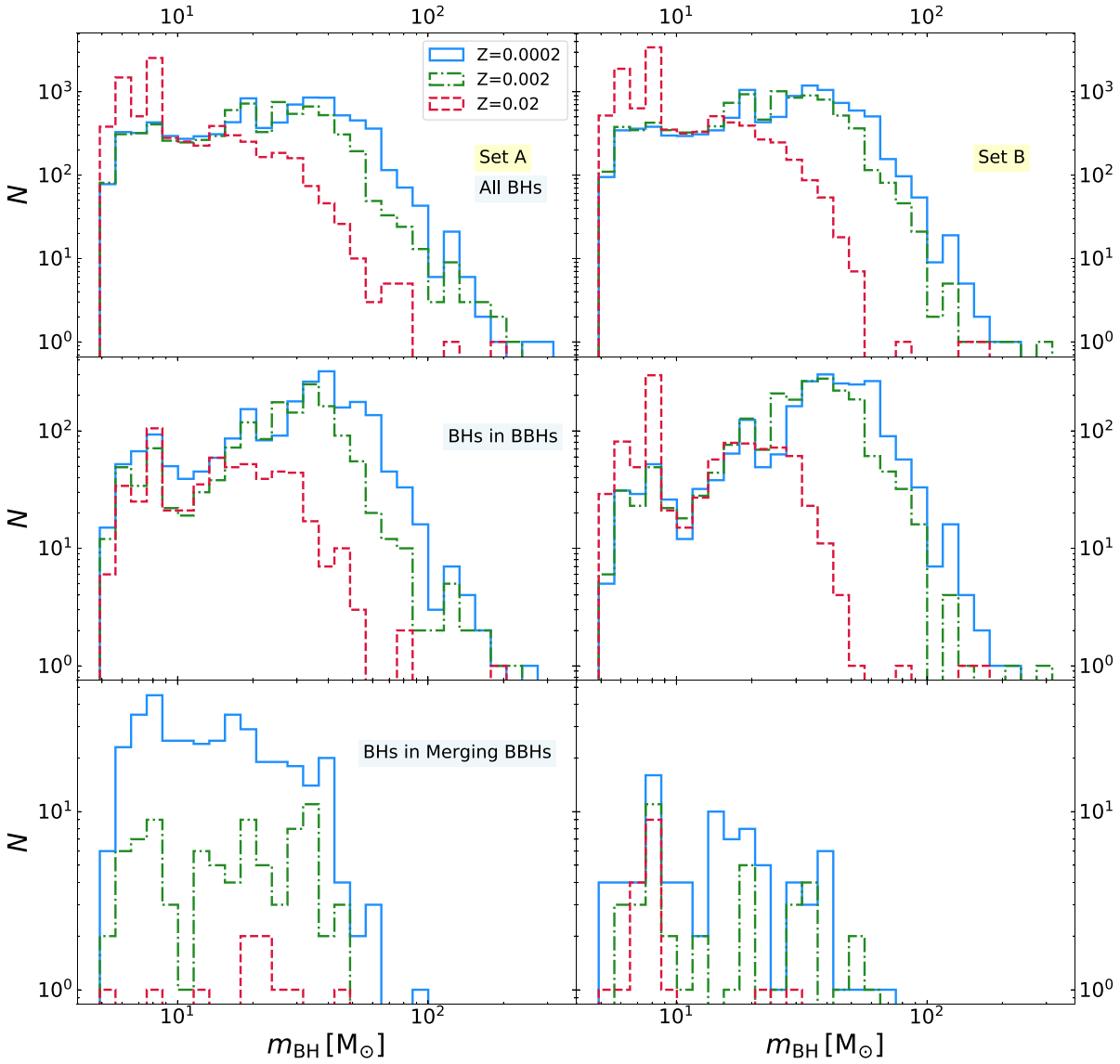

Figure 2. Distribution of BH masses in the simulations. Left-hand panels: set A; right-hand panels: set B. Top: all BHs; middle: BHs that are members of BBHs at the end of the simulations; bottom: BHs in merging BBHs. Blue solid line: $Z = 0.0002$; green dot–dashed line: $Z = 0.002$; red dashed line: $Z = 0.02$.

Table 2. Percentage of original and exchanged BBHs.

Set	$f_{\rm orig,all}$ (%)	$f_{\rm exch,all}$ (%)	$f_{\rm orig,merger}$ (%)	$f_{\rm exch,merger}$ (%)
YSC	22	78	58	42
A	18	82	58	42
B	25	75	65	35
A02	7	93	0	100
A002	15	85	36	64
A0002	24	76	65	35
B02	28	72	67	33
B002	22	78	75	25
B0002	25	75	60	40

Note. Column 1: name of the simulation set. Column 2: $f_{\rm orig,all}$, percentage of original BBHs with respect to all BBHs at the end of the simulations. Column 3: $f_{\rm exch,all}$, percentage of exchanged BBHs with respect to all BBHs at the end of the simulations. Column 4: $f_{\rm orig,merge}$, percentage of merging original BBHs with respect to all merging BBHs. Column 5: $f_{\rm exch,merge}$, percentage of merging exchanged BBHs with respect to all merging BBHs.

percentages of exchanged BBHs and merging exchanged BBHs are ∼76 and ∼35 per cent in set A0002, and rise to ∼93 and 100 per cent in set A02. In contrast, the percentages of exchanged BBHs and merging exchanged BBHs are ∼75 and ∼40 per cent in set B0002, and remain very similar (∼72 and 33 per cent) in set B02.

Table 3 shows the results of the Kolmogorov–Smirnov (hereafter, KS) test (Birnbaum & Tingey 1951; Marsaglia, Tsang & Wang 2003) and of the U-test (Bauer 1972; Hollander & Wolfe 1999). We find that the masses of merging BBHs in set A and in set B are not consistent with being drawn from two different underlying distributions. Based on this result and to filter out stochastic fluctuations, we consider BBH mergers of set A and set B together in the following analysis.

Figs 3, 4, and 5 show the total mass ($m_{\rm TOT} = m_1 + m_2$), the chirp mass [$m_{\rm chirp} = (m_1\, m_2)^{3/5}(m_1 + m_2)^{-1/5}$], and the mass ratio ($q = m_2/m_1$, where $m_1 \geq m_2$) of merging BBHs, respectively. In these figures, the three metallicity samples and the two simulation sets are stacked together.

Table 3. Results of the KS-test and U-test to compare sets of merging BBHs.

Set 1	Set 2	Distribution	KS-test	U-test
A – original	B – original	$m_{\rm tot}$	0.82	0.56
A – exchanged	B – exchanged	$m_{\rm tot}$	0.36	0.55
A – all	B – all	$m_{\rm tot}$	0.65	0.50
A – original	B – original	$m_{\rm chirp}$	0.57	0.35
A – exchanged	B – exchanged	$m_{\rm chirp}$	0.56	0.59
A – all	B – all	$m_{\rm chirp}$	0.33	0.38
A – original	B – original	q	0.05	0.14
A – exchanged	B – exchanged	q	0.84	0.59
A – all	B – all	q	0.50	0.54
A – original	B – original	$t_{\rm delay}$	0.43	0.35
A – exchanged	B – exchanged	$t_{\rm delay}$	0.99	0.94
A – all	B – all	$t_{\rm delay}$	0.88	0.50

Note. We apply the KS-test and U-test to compare different samples of BBHs. Columns 1 and 2: the two BBH samples to which we apply the KS-test and U-test. Each sample comes from one of the simulation sets (see Table 1). Column 3: distribution to which we apply the KS-test and U-test. We consider total BBH masses ($m_{\rm tot}$), chirp masses ($m_{\rm chirp}$), mass ratios (q), and delay times ($t_{\rm delay}$). Columns 4 and 5: probability that the two samples are drawn from the same distribution according to the KS-test and to the U-test, respectively.

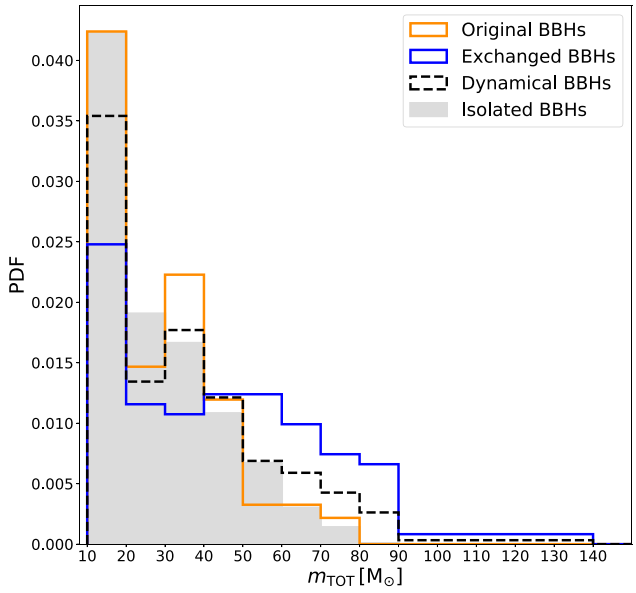

Figure 3. Distribution of total masses ($m_{\rm TOT} = m_1 + m_2$) of merging BBHs. Sets A and B are stacked together. Orange solid line: original BBHs; blue solid line: exchanged BBHs; black dashed line: all dynamical BBHs (original+exchanged); and grey filled histogram: isolated BBHs.

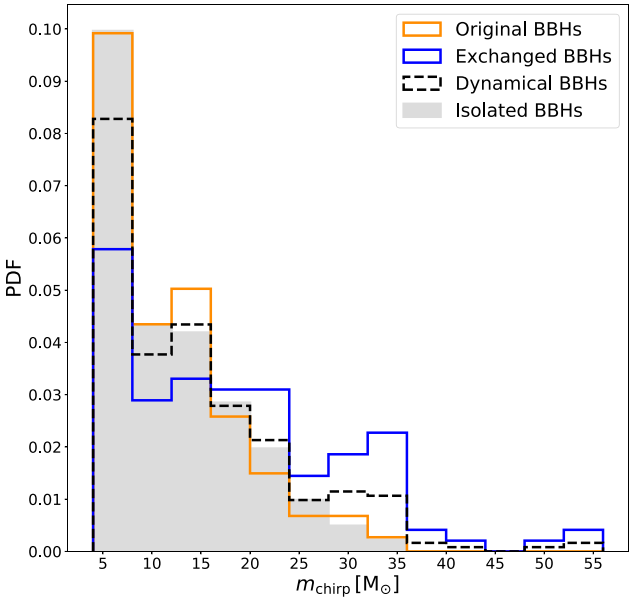

Figure 4. Same as Fig. 3, but for the distribution of chirp masses $m_{\rm chirp} = (m_1\, m_2)^{3/5}(m_1 + m_2)^{-1/5}$ of merging BBHs.

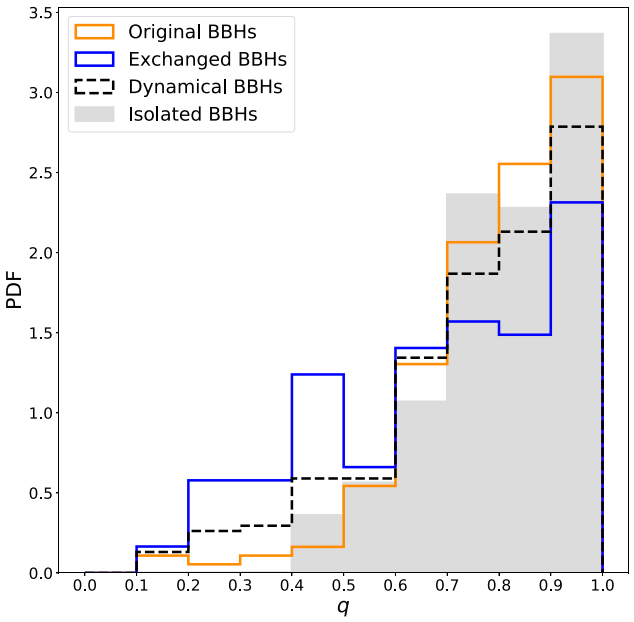

Figure 5. Same as Fig. 3, but for the distribution of mass ratios $q = m_2/m_1$ of merging BBHs.

The total masses of dynamical BBH mergers range from ∼10 to ∼140 M$_\odot$, while the chirp masses span from ∼4.8 to ∼55.8 M$_\odot$. Mass ratios of order of one are most common, but the distributions reach a minimum value of $q \sim 0.18$.

Exchanged BBHs reach significantly larger total masses and chirp masses and smaller values of q than both original BBHs and isolated BBHs. The typical masses of original BBHs are similar to those of isolated BBHs. This confirms the results of Di Carlo et al. (2019), who considered only one metallicity ($Z = 0.002$).

Fig. 6 shows the mass of the secondary BH (m_2) versus the mass of the primary BH (m_1), distinguishing between different metallicities. The most massive objects ($m_1 > 45$ M$_\odot$) form only at low metallicity ($Z = 0.0002$, 0.002) and are exclusively exchanged BBHs.

Table 4 shows the masses, metallicities, and delay times of BBH mergers with primary mass $m_1 \geq 45$ M$_\odot$. All of them are exchanged BBHs and (according to our population-synthesis model) cannot form by isolated binary evolution. We choose this threshold of 45 M$_\odot$, because Abbott et al. (2019b) indicate that the mass distribution of the primary BH in O1 and O2 LVC events is well approximated by models with no more than 1 per cent of BHs more massive than 45 M$_\odot$. In our simulations, we show that these BBH mergers are impossible to form via isolated binary evolution, but can arise

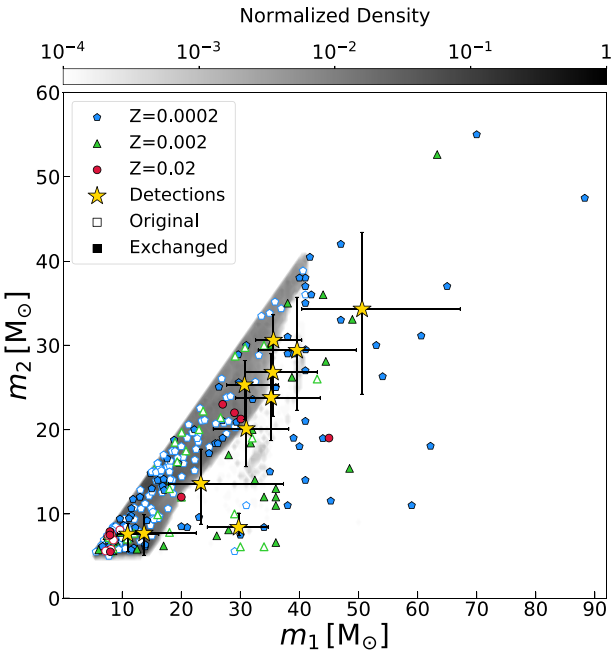

Figure 6. Mass of the primary BH (m_1) versus mass of the secondary BH (m_2) of merging BBHs. Sets A and B are stacked together. Empty symbols: original BBHs; filled symbols: exchanged BBHs. Blue, green, and red symbols represent $Z = 0.0002$, 0.002, and 0.02, respectively. Filled contours (with grey colour map): isolated BBHs. Yellow stars with error bars: LVC BBHs GW 150914 (Abbott et al. 2016b), GW 151012 (Abbott et al. 2016a), GW 151226 (Abbott et al. 2016c), GW 170104 (Abbott et al. 2017a), GW 170608 (Abbott et al. 2017c), GW 170729 (Abbott et al. 2019a), GW 170809 (Abbott et al. 2019a), GW 170814 (Abbott et al. 2017b), GW 170818 (Abbott et al. 2019a), GW 170823 (Abbott et al. 2019a), and GW 190412 (Abbott et al. 2020a). Error bars indicate 90 per cent credible levels.

Table 4. List of the BBH mergers with primary mass $m_1 \geq 45$ M$_\odot$ in our simulations.

m_1 (M$_\odot$)	m_2 (M$_\odot$)	q	Z	$t_{\rm delay}$ (Gyr)	Set
88.3	47.5	0.54	0.0002	0.046	A
70.0	55.0	0.79	0.0002	1.679	B
65.0	37.0	0.57	0.0002	0.0324	A
63.3	52.6	0.83	0.002	11.008	B
62.2	18.0	0.29	0.0002	0.264	B
60.6	31.1	0.51	0.0002	5.876	A
59.0	11.0	0.19	0.0002	0.499	A
54.1	26.3	0.49	0.0002	0.253	A
53.0	30.0	0.57	0.0002	7.0178	A
49.0	33.1	0.68	0.002	0.505	B
48.5	15.4	0.32	0.002	0.117	A
47.0	42.0	0.89	0.0002	0.0447	A
47.0	33.0	0.70	0.0002	0.437	B
45.3	11.5	0.25	0.0002	3.586	A
45.0	19.0	0.42	0.02	0.308	A

Note. Column 1: mass of the primary BH (m_1). Column 2: mass of the secondary BH (m_2). Column 3: mass ratio (q). Column 4: progenitor's metallicity (Z). Column 5: delay time ($t_{\rm delay}$). Column 6: simulation set.

from dynamical exchanges in YSCs. These massive BBH mergers are 4.3 and 7.0 per cent of all the BBH mergers we find in set A and set B, respectively. Most of them have mass ratios different from one.

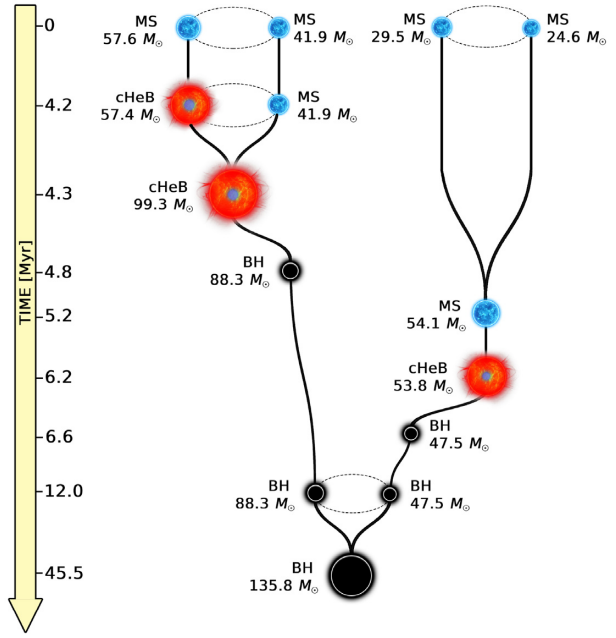

Figure 7. Evolution of the most massive BBH merger in our simulations. Blue stars represent main-sequence stars (with label MS); red stars with a blue core represent core helium burning stars (label cHeB); black circles represent black holes (label BH). The mass of each object is shown next to them. The time axis and the size of the objects are not to scale. The primary BH with $m_1 = 88.3$ M$_\odot$ lies in the pair-instability mass gap. The merging BBH forms because of dynamical interactions.

Fig. 7 shows the evolution of the most massive BBH merger in our simulations, with a primary mass $m_1 = 88$ M$_\odot$ and a secondary mass $m_2 = 48$ M$_\odot$. Both the primary and the secondary BH in this system form from the merger of two progenitor stars and become bound by exchange. The mass of the primary BH is within the pair-instability mass gap. This happens because the merger between a core helium burning (cHeB) star and a main-sequence (MS) star produces a new cHeB star with a large hydrogen envelope and with a helium core below the threshold for (pulsational) pair instability (see Di Carlo et al. 2020 for further details). The merger between the 57.4 M$_\odot$ cHeB and the 41.9 M$_\odot$ MS is triggered by a dynamical encounter. If we simulate a binary with the same initial conditions using the stand-alone version of MOBSE (i.e. without dynamical perturbations), the binary does not merge at 4.3 Myr and leaves a smaller remnant.

The yellow stars in Fig. 6 show the 10 BBHs detected by the LVC during O1 and O2 (Abbott et al. 2019a) plus GW 190412, the first published BBH merger of O3 and the first event showing evidence of unequal-mass components (Abbott et al. 2020a). Our simulated BBH mergers match all O1–O2 BBHs including GW 170729. GW 170729, the most massive event detected in O1 and O2, is consistent only with BBHs formed in YSCs (mostly exchanged BBHs): our models cannot form GW 170729 via isolated binary evolution, even at the lowest considered metallicity. This result strongly favours a dynamical formation for GW 170729. Even GW 190412 can be matched only by dynamical BBHs born from metal-poor progenitors, because isolated binaries can hardly account for its mass ratio in our models.

Fig. 8 shows the distribution of delay times for our simulated BBHs. We find no significant differences between the delay time distribution of set A and set B (see Table 3). The two distributions are broadly consistent with $\mathrm{d}N/\mathrm{d}t \propto t^{-1}$ (Dominik et al. 2012) if $t_{\rm delay} \gtrsim 400$ Myr, but bend with respect to this scaling at shorter

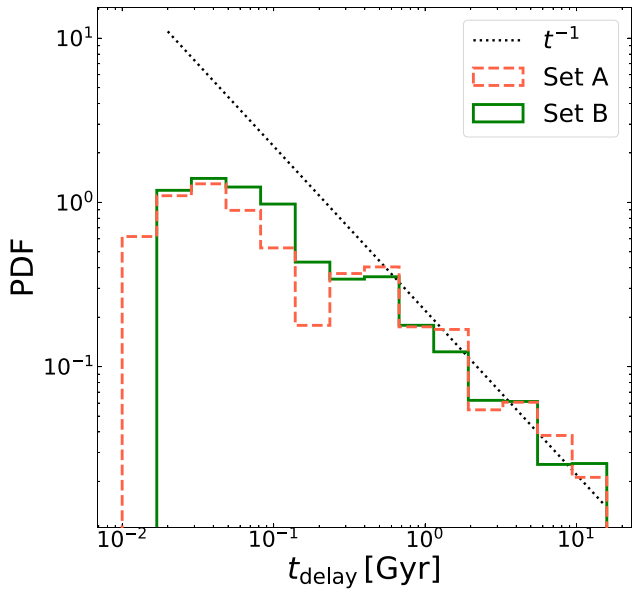

Figure 8. Distribution of delay times $t_{\rm delay}$ of merging BBHs. Orange dashed line: set A; green solid line: set B; and dotted black line: scaling as $\mathrm{d}N/\mathrm{d}t \propto t^{-1}$.

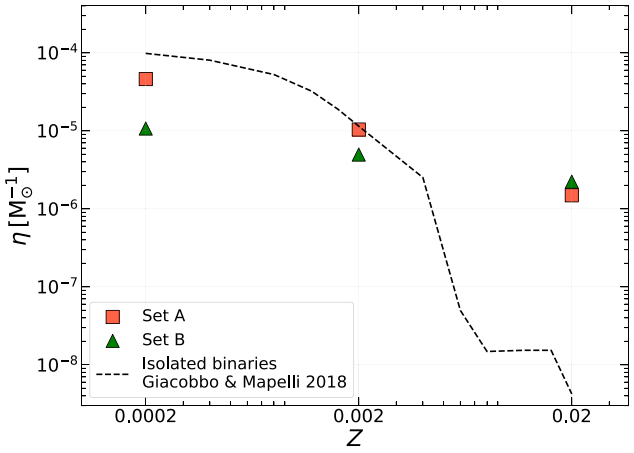

Figure 9. Merger efficiency $\eta(Z)$, defined as the number of mergers per solar mass, as a function of metallicity. The black dashed line shows the values from Giacobbo & Mapelli (2018). Orange squares and green triangles refer to set A and set B, respectively.

times. As a result, the overall distributions are not consistent with $\propto t^{-1}$, unless we neglect delay times shorter than 400 Myr.

3.3 Merger efficiency and local merger rate

Fig. 9 shows the merger efficiency $\eta(Z)$ defined as in Giacobbo & Mapelli (2018):

$$\eta(Z) = \frac{N_{\rm TOT}(Z)}{M_*(Z)}, \tag{3}$$

where $N_{\rm TOT}(Z)$ is the total number of BBHs (formed at a given metallicity) with delay time shorter than the Hubble time, while $M_*(Z)$ is the total initial stellar mass of the simulated population at a given metallicity. For isolated binaries (Giacobbo & Mapelli 2018), $M_*(Z) = M_{*,\rm sim}(Z)/(f_{\rm bin}\, f_{\rm corr})$, where $M_{*,\rm sim}(Z)$ is the total initial mass of the simulated binaries, $f_{\rm bin} = 0.4$ accounts for the fact that we simulated only binaries and not single stars, and $f_{\rm corr}$ accounts for the missing low-mass stars between 0.1 and 5 $\mathrm{M}_\odot$. The merger efficiency is a useful quantity to understand the impact of stellar metallicity on the merger rate of binary compact objects.

The most remarkable difference between isolated BBHs and dynamical BBHs is that, at solar metallicity ($Z = 0.02$), the merger efficiency of the latter is higher by two orders of magnitude than the merger efficiency of the former. In YSCs, exchanges lead to the formation of BBHs and dynamical encounters harden existing massive binary stars, even at solar metallicity. In contrast, isolated BBH mergers are much rarer at solar metallicity, because stellar winds are efficient: the vast majority of massive stars become Wolf–Rayet stars before they can start a Roche lobe episode and do not undergo a common envelope phase; hence, most of the isolated BBHs that form at solar metallicity are too wide to merge within a Hubble time (Giacobbo & Mapelli 2018).

From the merger efficiency $\eta(Z)$, we can estimate the local merger rate density $\mathcal{R}_{\rm BBH}$, as already described in Santoliquido et al. (2020):

$$\mathcal{R}_{\rm BBH} = \frac{1}{t_{\rm lb}(z_{\rm loc})} \int_{z_{\rm max}}^{z_{\rm loc}} \psi(z') \frac{\mathrm{d}t_{\rm lb}}{\mathrm{d}z'} \mathrm{d}z' \times \int_{Z_{\rm min}(z')}^{Z_{\rm max}(z')} \eta(Z)\, \mathcal{F}(z', z_{\rm loc}, Z)\, \mathrm{d}Z, \tag{4}$$

where $t_{\rm lb}(z_{\rm loc})$ is the lookback time evaluated in the local universe ($z_{\rm loc} \leq 0.1$), $\psi(z')$ is the cosmic star formation rate density at redshift z' (from Madau & Fragos 2017), $Z_{\rm min}(z')$ and $Z_{\rm max}(z')$ are the minimum and maximum metallicity of stars formed at redshift z' and $\mathcal{F}(z_{\rm loc}, z', Z)$ is the fraction of BBHs that form at redshift z' from stars with metallicity Z and merge at redshift $z_{\rm loc}$ normalized to all BBHs that form from stars with metallicity Z. To calculate the lookback time $t_{\rm lb}$ we take the cosmological parameters (H_0, $\Omega_{\rm M}$, and Ω_Λ) from Ade et al. (2016). We integrate equation (4) up to redshift $z_{\rm max} = 15$, which we assume to be the epoch of formation of the first stars.

From equation (4) we obtain a local merger rate density $\mathcal{R}_{\rm BBH} \sim 55$ and ~ 110 Gpc^{-3} yr^{-1} for set A and set B, respectively, by assuming that all the cosmic star formation rate occurs in YSCs like the ones we simulated in this paper. If we repeat the same procedure for the isolated BBHs, we find $\mathcal{R}_{\rm BBH} \sim 50$ Gpc^{-3} yr^{-1}. Set B gives the highest local merger rate density, because it has a higher number of BBH mergers at solar metallicity (which is the dominant metallicity at low redshift) with relatively short delay times. Considering the small sample of BBH mergers at $Z = 0.02$ (five BBHs in set A and eight BBHs in set B), the difference of a factor of 2 between the two local merger rates is likely due to stochastic fluctuations.

The inferred merger rates are upper limits, since we do not take into account infant mortality of YSCs (Brinkmann et al. 2017; Shukirgaliyev et al. 2017), we do not use an observation-based local number density of YSCs (Portegies Zwart & McMillan 2000) and we assume that all stars form in YSCs like the ones we simulated in this paper. It is more likely that a fraction of all mergers come from YSCs and another fraction from isolated binaries, globular clusters, or nuclear star clusters. In a follow-up paper (Bouffanais et al., in preparation), we will try to constrain these percentages based on current LVC results.

4 DISCUSSION

4.1 Merger efficiency: dynamical versus isolated BBHs

Why the merger efficiency of dynamical BBHs is lower than that of isolated BBHs at low metallicity, but higher at high metallicity? This result springs from two opposite effects. On the one hand, dynamical encounters tend to break some BBHs, especially low-mass BBHs with a relatively large orbital separation (see e.g. Zevin et al. 2017;

Table 5. Progenitors of exchanged BBH mergers at the time of the first exchange.

Set	$f_{\rm star-star}$ (%)	$f_{\rm star-BH}$ (%)	$f_{\rm BBH}$ (%)
YSC	57	12	31
A	54	14	32
B	72	0	28
A02	0	0	100
A002	45	9	46
A0002	60	17	23
B02	67	0	33
B002	60	0	40
B0002	80	0	20

Note. Column 1: simulation set. Column 2: percentage of exchanged BBH mergers in which the result of the first exchange is a star–star binary ($f_{\rm star-star}$). Column 3: percentage of exchanged BBH mergers in which the result of the first exchange is a star–BH binary ($f_{\rm star-BH}$). Column 4: percentage of exchanged BBH mergers in which the outcome of the first exchange is already a BBH ($f_{\rm BBH}$).

Di Carlo et al. 2019). On the other hand, dynamics enhances the merger of massive BBHs by exchanges and by hardening. The former effect tends to decrease the merger efficiency, while the latter tends to increase it.

At solar metallicity ($Z = 0.02$), the merger efficiency of isolated BBHs is drastically low (2–3 orders of magnitude lower than at $Z \leq 0.002$). This implies that, at solar metallicity, even if dynamics ionizes all the low-mass original BBHs, this has no effect on the merger efficiency, because these low-mass original BBHs were not going to merge anyway. Thus, the loss of BBH mergers due to binary ionization/softening is minimum at high Z. In contrast, the few dynamical BBH mergers at high Z all come from dynamical hardening and dynamical exchanges. The net effect is that the merger efficiency of dynamical BBHs is higher than that of isolated BBHs at solar metallicity.

At low Z, the situation is inverted. Most of the mergers from isolated BBHs come from low-mass BBHs (see e.g. Giacobbo et al. 2018). Hence, when dynamics suppresses the merger of these low-mass BBHs (by softening or ionization), it removes most of potential merging systems from the game. In metal-poor clusters, dynamical hardening and exchanges are efficient in forming massive BBHs and in triggering their merger, but these massive binaries are not sufficiently numerous to compensate for the loss of low-mass mergers. Hence, the net effect is that the merger efficiency of dynamical BBHs is lower than that of isolated BBHs at low Z.

There is also a difference between set A (dense clusters) and set B (loose clusters). At low Z, the merger efficiency of set A is a factor of ∼5 higher than that of set B, while at higher Z the two sets have almost the same merger efficiency. The main reason for this difference is that, at low Z, where BH masses are higher, dynamical hardening and exchanges are more effective in the dense clusters of set A than in the loose clusters of set B.

4.2 When do the exchanges happen?

Table 5 shows that most of the exchanged BBHs that merge within a Hubble time undergo their first exchange when the binary system is still composed of two stars, i.e. before the collapse of the primary component to a BH. The percentage of exchanges whose result is a binary composed of two stars are ∼54 and ∼72 per cent for set A and set B, respectively.

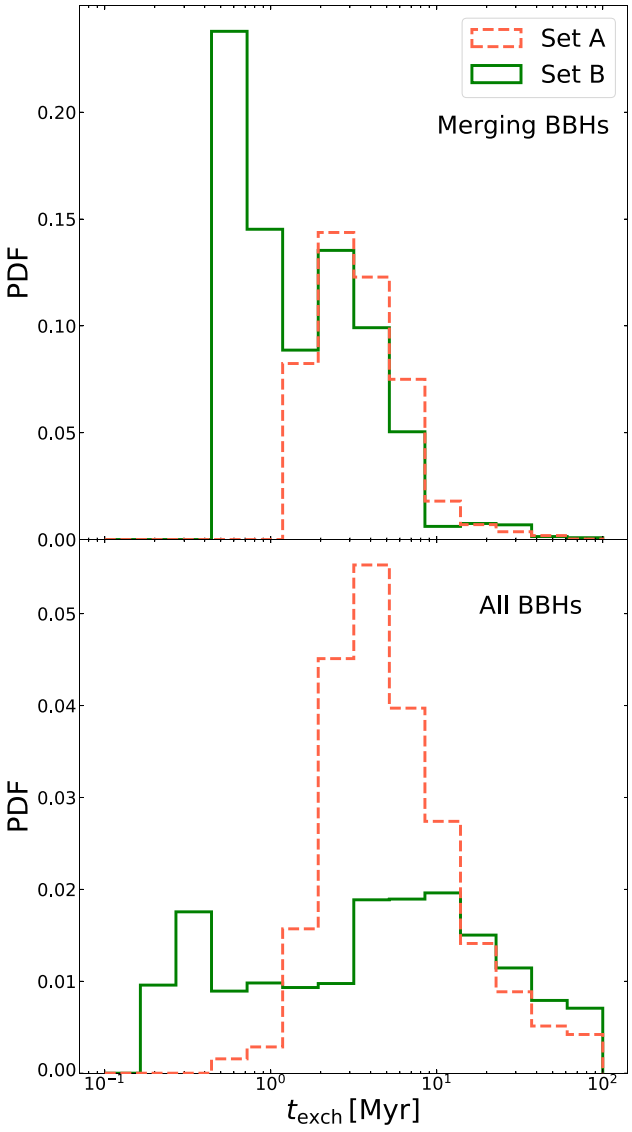

Figure 10. Time when the first exchange took place for exchanged BBHs in set A (orange dashed line) and set B (green solid line). Top panel: merging BBHs only. Bottom panel: all BBHs.

The percentage of exchanges that lead to the formation of a BH–star binary are zero in set B and up to ∼17 per cent in set A. Finally, ∼30 per cent of all exchanges that lead to BBH mergers happen when the two BHs have already formed.

Fig. 10 confirms this result: the dynamical exchanges that lead to the formation of merging systems happen in the first ∼10 Myr of the star cluster life. Most of these exchanges happen earlier ($t \ll 1$ Myr) in the star clusters of set B than in those of set A ($t \sim 2$–3 Myr).

This reflects a difference in the time-scale for the collapse of the core of the cluster (hereafter, core collapse), because most interactions happen during core collapse. In set B, the single subclumps of our fractal initial conditions undergo core collapse before they have completed the hierarchical assembly into the larger star cluster. Hence, most exchanges and dynamical interactions happen in this very early stage, $t < 1$ Myr. In contrast, the clusters of set A are so dense that the subclumps hierarchically assemble to form one

monolithic cluster before they undergo individual core collapse. Hence, the first core collapse in set A is the collapse of the core of the global cluster at $t \sim 2$–3 Myr. As already discussed by Fujii & Portegies Zwart (2013), the build-up and merger of massive binaries are suppressed if the subclumps collapse before the hierarchical assembly of the global cluster. Hence, we expect the binaries of set A to start their dynamical activity later but to have more dynamical interactions with respect to the binaries of set B.

4.3 Integration time and merger rates

We integrated all the simulated YSCs until their dissolution or for a maximum time $t = 100$ Myr. Would a longer integration time significantly affect the number of mergers? At the end of the simulations, our YSCs retain between 50 and 70 per cent of their initial mass and ∼60 per cent of the total BBHs. However, the vast majority of these in-cluster BBHs are loose binaries (∼99.5 per cent of them have an orbital separation $a > 10^2$ R$_\odot$) and would therefore require many strong dynamical interactions to harden and enter the gravitational wave regime. In a future work, we will integrate our clusters up to 1 Gyr to check the impact of the integration time on BBHs, but we do not expect it to significantly affect the number of mergers.

4.4 Comparison with previous studies

Kumamoto et al. (2019, 2020) evaluate the BBH merger rate from open clusters, whose masses and scales are comparable to our fractal YSCs. Kumamoto et al. (2019) find that exchanges leading to BBH mergers happen mostly between stellar progenitors (before their collapse to BH), consistently with our results (see also Di Carlo et al. 2019). Moreover, Kumamoto et al. (2020) predict a local BBH merger rate density ∼35 Gpc^{-3} yr^{-1}, similar to our result. Banerjee (2020) produced a set of simulations of more massive YSC, with masses between 10^4 and 10^5 M$_\odot$ and with lower binary fractions ($0 < f_{\rm bin} < 0.1$). Banerjee (2020) finds a mass spectrum of merging BBHs that is similar to our result; the main difference is that we find systems with lower mass ratios. Moreover, while 97 per cent of our BBH mergers take place outside the YSC, most of the mergers in Banerjee (2017, 2020) happen inside the cluster, likely because of the higher star cluster mass in these studies with respect to our simulations.

These results for both YSCs (Di Carlo et al. 2019, 2020) and open clusters (Banerjee et al. 2010; Ziosi et al. 2014; Banerjee 2017, 2018) remark a crucial difference with respect to globular clusters (e.g. Portegies Zwart & McMillan 2000; Morscher et al. 2015; Rodriguez et al. 2015, 2016, 2018; Askar et al. 2017) and nuclear star clusters (e.g. Antonini & Rasio 2016; Arca Sedda & Benacquista 2019). Globular and nuclear clusters are significantly more long-lived than open and young clusters. Hence, BBHs born in the former clusters have more time to harden by gravitational encounters and to undergo exchanges before they merge. This is expected to boost the merger efficiency per globular/nuclear cluster. On the other hand, most globular clusters formed ∼12 Gyr ago; hence, their contribution to the *local* merger rate density is relatively small (<20 Gpc^{-3} yr^{-1}; e.g. Askar et al. 2017; Rodriguez & Loeb 2018).

In contrast, YSCs are short-lived, but form all the time across cosmic history. Thus, they might have a larger cumulative effect on the local merger rate density of BBHs. Moreover, YSCs are the main birthplace of massive stars, and, when they are disrupted by gas evaporation or by the tidal field, they release their stellar content into the field. Thus, a large fraction of the field binaries might have formed in an YSC and might have taken part in dynamical encounters before their ejection/evaporation (Kruijssen 2012).

A further difference between BBHs born in globular clusters and YSCs is the location of the mergers. About half of BBHs born in globular clusters are expected to merge inside the cluster (Banerjee 2017; Rodriguez et al. 2018; Samsing 2018; Zevin et al. 2019). In contrast, ∼97 per cent of our merging BBHs reach coalescence after they were ejected from the YSC, because of the low escape velocity and of the short lifetime of these systems. Hence, most BBHs born in YSCs merge in the galactic field and might represent a large fraction of field mergers.

5 CONCLUSIONS

We have investigated the formation of BBH mergers in YSCs with different metallicity, from $Z = 0.0002$ to 0.02, by means of *N*-body simulations, coupled with the binary population-synthesis code MOBSE (Giacobbo et al. 2018; Di Carlo et al. 2019). We probe two different density regimes for YSCs: dense clusters (set A, i.e. clusters with half-mass radius following the Marks et al. 2012 relation, corresponding to a density $\rho_{\rm h} \geq 3.4 \times 10^4$ M$_\odot$ pc^{-3}) and loose clusters (set B, i.e. clusters with half-mass radius $r_{\rm h} = 1.5$ pc, corresponding to a density $\rho_{\rm h} \geq 1.5 \times 10^2$ M$_\odot$ pc^{-3}, depending on star cluster mass).

We have shown that BHs and BBHs can reach higher masses at lower metallicity ($Z \leq 0.002$) with respect to solar metallicity (Fig. 2). In our simulations, we can form IMBHs as massive as ∼320 M$_\odot$ through multiple stellar collisions. Stellar collisions also allow the formation of BHs with mass in the pair-instability mass gap (Di Carlo et al. 2020) even at solar metallicity, although their incidence is much higher at low metallicity ($Z \leq 0.002$). We find that ∼6 per cent (∼2 per cent) of all BHs formed at $Z = 0.0002$ ($Z = 0.002$) have mass $m_{\rm BH} > 60$ M$_\odot$, while at solar metallicity ($Z = 0.02$) the percentage is <1 per cent in both set A and set B.

The mass function of BHs and BBHs does not show significant differences between loose clusters (set B) and dense clusters (set A). In particular, IMBHs form nearly with the same frequency in both loose and dense clusters.

We focus on the subsample of BBHs that merge within a Hubble time. About 60 per cent of them come from original binaries (i.e. binary stars that are already there in the initial conditions), while the remaining ∼40 per cent form from dynamical exchanges. Exchanges in YSCs mostly involve stars before they collapse to BHs, because of the short core-collapse time-scale of YSCs (<3 Myr).

Exchanged BBH mergers reach higher total masses (up to ∼140 M$_\odot$) than original and isolated BBH mergers (maximum total mass ∼80 M$_\odot$, Fig. 3). The reason is that non-conservative mass transfer tends to reduce the maximum mass of BBH mergers in isolated and original binaries. Moreover, exchanged BBHs tend to have lower mass ratios ($q = m_2/m_1$) than original and isolated BBHs (Fig. 5).

In our models, the most massive event reported by the LVC in O1 and O2, GW 170729 (Abbott et al. 2019a,b), can be explained only with dynamical BBHs: almost all of them are exchanged BBHs and come from metal-poor progenitors (Fig. 6). Even GW 190412, the first unequal-mass BBH merger, can be explained only by BBHs born in YSCs: isolated binaries can hardly explain such extreme mass ratios, according to the models presented here.

The most massive BBH merger in our simulations has $m_{\rm TOT} \sim 136$ M$_\odot$, primary mass $m_1 \sim 88$ M$_\odot$, and secondary mass $m_2 \sim 48$ M$_\odot$ (Table 4). The primary mass is inside the pair-instability

mass gap and the total mass of the merger product classifies it as in IMBH. This system is more massive than all the O1 and O2 LVC BBHs.

The merger efficiency (i.e. the number of mergers divided by the total simulated mass) is about two orders of magnitude higher for dynamical BBHs than for isolated BBHs at solar metallicity (Fig. 9). The main reason is that dynamical encounters and hardening trigger the merger of BBHs even at high metallicity, where binary evolution is unlikely to produce mergers.

The main difference between loose and dense clusters is the merger efficiency. At low metallicity, the merger efficiency of loose clusters is a factor of ∼5 lower than that of dense cluster, while at higher metallicity the merger efficiencies are comparable. Assuming that all the cosmic star formation rate takes place in YSCs, we find a local merger rate ∼55 (∼110) Gpc^{-3} yr^{-1} in set A (set B), respectively. This shows that most BBH mergers might have originated in YSCs. Future studies will quantify the impact of YSCs on the total merger rate of BBHs, BHNSs, and BNSs, based on the comparison with LVC observations.

ACKNOWLEDGEMENTS

We are grateful to the anonymous referee for careful reading of the manuscript and useful comments. We thank Astrid Lamberts, Long Wang, and Serena Banfi for useful comments. UNDC acknowledges financial support from Università degli Studi dell'Insubria through a Cycle 33rd PhD grant. MM, NG, YB, SR, FS, and AB acknowledge financial support from the European Research Council (ERC) under European Union's Horizon 2020 research and innovation programme, grant agreement no. 770017 (DEMOBLACK ERC Consolidator Grant). MS acknowledges funding from the European Union's Horizon 2020 research and innovation programme under the Marie-Sklodowska-Curie grant agreement no. 794393. AAT acknowledges support from JSPS KAKENHI Grant Numbers 17F17764 and 17H06360. UNDC and AAT also thank the Center for Interdisciplinary Exploration and Research in Astrophysics at Northwester University for its hospitality. This work benefited from support by the International Space Science Institute (ISSI), Bern, Switzerland, through its International Team programme reference no. 393, The Evolution of Rich Stellar Populations & BH Binaries (2017–18).

DATA AVAILABILITY

The data underlying this paper will be shared on reasonable request to the corresponding authors.

REFERENCES

Aarseth S. J., 2003, Gravitational N-Body Simulations. Cambridge Univ. Press, Cambridge
Aasi J. et al., 2015, Classical Quantum Gravity, 32, 074001
Abbott B. P. et al., 2016a, Phys. Rev. X, 6, 041015
Abbott B. P. et al., 2016b, Phys. Rev. Lett., 116, 061102
Abbott B. P. et al., 2016c, Phys. Rev. Lett., 116, 241103
Abbott B. P. et al., 2016d, ApJ, 818, L22
Abbott B. P. et al., 2017a, Phys. Rev. Lett., 118, 221101
Abbott B. P. et al., 2017b, Phys. Rev. Lett., 119, 141101
Abbott B. P. et al., 2017c, ApJ, 851, L35
Abbott B. P. et al., 2019a, Phys. Rev. X, 9, 031040
Abbott B. P. et al., 2019b, ApJ, 882, L24
Abbott B. P. et al., 2020a, preprint (arXiv:2004.08342)
Abbott B. P. et al., 2020b, ApJ, 892, L3
Acernese F. et al., 2015, Classical Quantum Gravity, 32, 024001
Ade P. A. R. et al., 2016, A&A, 594, A13
Antonini F., Rasio F. A., 2016, ApJ, 831, 187
Antonini F., Gieles M., Gualandris A., 2019, MNRAS, 486, 5008
Arca Sedda M., Benacquista M., 2019, MNRAS, 482, 2991
Arca-Sedda M., Gualandris A., 2018, MNRAS, 477, 4423
Arca Sedda M., Mapelli M., Spera M., Benacquista M., Giacobbo N., 2020, ApJ, 894, 133
Askar A., Szkudlarek M., Gondek-Rosińska D., Giersz M., Bulik T., 2017, MNRAS, 464, L36
Askar A., Arca Sedda M., Giersz M., 2018, MNRAS, 478, 1844
Baibhav V., Berti E., Gerosa D., Mapelli M., Giacobbo N., Bouffanais Y., Di Carlo U. N., 2019, Phys. Rev. D, 100, 064060
Ballone A., Mapelli M., Di Carlo U. N., Torniamenti S., Spera M., Rastello S., 2020, MNRAS, 496, 49
Banerjee S., 2017, MNRAS, 467, 524
Banerjee S., 2018, MNRAS, 473, 909
Banerjee S., 2020, preprint (arXiv:2004.07382)
Banerjee S., Baumgardt H., Kroupa P., 2010, MNRAS, 402, 371
Bauer D. F., 1972, J. Am. Stat. Assoc., 67, 687
Belczynski K., Kalogera V., Bulik T., 2002, ApJ, 572, 407
Belczynski K., Kalogera V., Rasio F. A., Taam R. E., Zezas A., Bulik T., Maccarone T. J., Ivanova N., 2008, ApJS, 174, 223
Belczynski K., Bulik T., Fryer C. L., Ruiter A., Valsecchi F., Vink J. S., Hurley J. R., 2010, ApJ, 714, 1217
Belczynski K., Holz D. E., Bulik T., O'Shaughnessy R., 2016, Nature, 534, 512
Bethe H. A., Brown G. E., 1998, ApJ, 506, 780
Birnbaum Z., Tingey F. H., 1951, Ann. Math. Stat., 22, 592
Bouffanais Y., Mapelli M., Gerosa D., Di Carlo U. N., Giacobbo N., Berti E., Baibhav V., 2019, ApJ, 886, 25
Brinkmann N., Banerjee S., Motwani B., Kroupa P., 2017, A&A, 600, A49
Burrows A., Vartanyan D., Dolence J. C., Skinner M. A., Radice D., 2018, Space Sci. Rev., 214, 33
Carr B. J., Hawking S. W., 1974, MNRAS, 168, 399
Carr B., Kühnel F., Sandstad M., 2016, Phys. Rev. D, 94, 083504
Cartwright A., Whitworth A. P., 2004, MNRAS, 348, 589
Chen Y., Bressan A., Girardi L., Marigo P., Kong X., Lanza A., 2015, MNRAS, 452, 1068
Choksi N., Volonteri M., Colpi M., Gnedin O. Y., Li H., 2019, ApJ, 873, 100
Claeys J. S. W., Pols O. R., Izzard R. G., Vink J., Verbunt F. W. M., 2014, A&A, 563, A83
de Mink S. E., Mandel I., 2016, MNRAS, 460, 3545
Di Carlo U. N., Giacobbo N., Mapelli M., Pasquato M., Spera M., Wang L., Haardt F., 2019, MNRAS, 487, 2947
Di Carlo U. N., Mapelli M., Bouffanais Y., Giacobbo N., Santoliquido F., Bressan A., Spera M., Haardt F., 2020, MNRAS, 497, 1043
Dominik M., Belczynski K., Fryer C., Holz D. E., Berti E., Bulik T., Mandel I., O'Shaughnessy R., 2012, ApJ, 759, 52
Dominik M., Belczynski K., Fryer C., Holz D. E., Berti E., Bulik T., Mandel I., O'Shaughnessy R., 2013, ApJ, 779, 72
Downing J. M. B., Benacquista M. J., Giersz M., Spurzem R., 2010, MNRAS, 407, 1946
Downing J. M. B., Benacquista M. J., Giersz M., Spurzem R., 2011, MNRAS, 416, 133
Farmer R., Renzo M., de Mink S. E., Marchant P., Justham S., 2019, ApJ, 887, 53
Fishbach M., Holz D. E., Farr B., 2017, ApJ, 840, L24
Fryer C. L., Belczynski K., Wiktorowicz G., Dominik M., Kalogera V., Holz D. E., 2012, ApJ, 749, 91
Fujii M. S., Portegies Zwart S., 2013, MNRAS, 430, 1018
Fujii M. S., Tanikawa A., Makino J., 2017, PASJ, 69, 94
Gerosa D., Berti E., 2017, Phys. Rev. D, 95, 124046
Gerosa D., Berti E., 2019, Phys. Rev. D, 100, 041301
Gerosa D., Berti E., O'Shaughnessy R., Belczynski K., Kesden M., Wysocki D., Gladysz W., 2018, Phys. Rev. D, 98, 084036
Giacobbo N., Mapelli M., 2018, MNRAS, 480, 2011
Giacobbo N., Mapelli M., 2019, MNRAS, 482, 2234

Giacobbo N., Mapelli M., 2020, ApJ, 891, 141
Giacobbo N., Mapelli M., Spera M., 2018, MNRAS, 474, 2959
Gieles M., Portegies Zwart S. F., Baumgardt H., Athanassoula E., Lamers H. J. G. L. M., Sipior M., Leenaarts J., 2006, MNRAS, 371, 793
Giersz M., Leigh N., Hypki A., Lützgendorf N., Askar A., 2015, MNRAS, 454, 3150
Goodwin S. P., Whitworth A. P., 2004, A&A, 413, 929
Goswami S., Kiel P., Rasio F. A., 2014, ApJ, 781, 81
Gräfener G., Hamann W.-R., 2008, A&A, 482, 945
Gutermuth R. A., Megeath S. T., Pipher J. L., Williams J. P., Allen L. E., Myers P. C., Raines S. N., 2005, ApJ, 632, 397
Hoang B.-M., Naoz S., Kocsis B., Rasio F. A., Dosopoulou F., 2018, ApJ, 856, 140
Hobbs G., Lorimer D. R., Lyne A. G., Kramer M., 2005, MNRAS, 360, 974
Hollander M., Wolfe D. A., 1999, Nonparametric Statistical Methods, 2nd edn. Wiley, Chichester
Hurley J. R., Pols O. R., Tout C. A., 2000, MNRAS, 315, 543
Hurley J. R., Tout C. A., Pols O. R., 2002, MNRAS, 329, 897
Hurley J. R., Sippel A. C., Tout C. A., Aarseth S. J., 2016, Publ. Astron. Soc. Aust., 33, e036
Kroupa P., 2001, MNRAS, 322, 231
Kruckow M. U., Tauris T. M., Langer N., Kramer M., Izzard R. G., 2018, MNRAS, 481, 1908
Kruijssen J. M. D., 2012, MNRAS, 426, 3008
Kumamoto J., Fujii M. S., Tanikawa A., 2019, MNRAS, 486, 3942
Kumamoto J., Fujii M. S., Tanikawa A., 2020, MNRAS, 495, 4268
Küpper A. H. W., Maschberger T., Kroupa P., Baumgardt H., 2011, MNRAS, 417, 2300
Lada C. J., Lada E. A., 2003, ARA&A, 41, 57
McKernan B., Ford K. E. S., Lyra W., Perets H. B., 2012, MNRAS, 425, 460
McKernan B. et al., 2018, ApJ, 866, 66
Madau P., Fragos T., 2017, ApJ, 840, 39
Makino J., Aarseth S. J., 1992, PASJ, 44, 141
Mandel I., de Mink S. E., 2016, MNRAS, 458, 2634
Mapelli M., 2016, MNRAS, 459, 3432
Mapelli M., Giacobbo N., 2018, MNRAS, 479, 4391
Mapelli M., Zampieri L., 2014, ApJ, 794, 7
Mapelli M., Colpi M., Zampieri L., 2009, MNRAS, 395, L71
Mapelli M., Ripamonti E., Zampieri L., Colpi M., Bressan A., 2010, MNRAS, 408, 234
Mapelli M., Zampieri L., Ripamonti E., Bressan A., 2013, MNRAS, 429, 2298
Mapelli M., Giacobbo N., Ripamonti E., Spera M., 2017, MNRAS, 472, 2422
Mapelli M., Giacobbo N., Santoliquido F., Artale M. C., 2019, MNRAS, 487, 2
Mapelli M., Spera M., Montanari E., Limongi M., Chieffi A., Giacobbo N., Bressan A., Bouffanais Y., 2020, ApJ, 888, 76
Marchant P., Langer N., Podsiadlowski P., Tauris T. M., Moriya T. J., 2016, A&A, 588, A50
Marchant P., Renzo M., Farmer R., Pappas K. M. W., Taam R. E., de Mink S. E., Kalogera V., 2019, ApJ, 882, 36
Marks M., Kroupa P., Dabringhausen J., Pawlowski M. S., 2012, MNRAS, 422, 2246
Marsaglia G., Tsang W. W., Wang J., 2003, J. Stat. Softw., 8, 1
Mennekens N., Vanbeveren D., 2014, A&A, 564, A134
Mikkola S., Aarseth S. J., 1993, Celest. Mech. Dyn. Astron., 57, 439
Miller M. C., Hamilton D. P., 2002, MNRAS, 330, 232
Miller M. C., Lauburg V. M., 2009, ApJ, 692, 917
Moe M., Di Stefano R., 2017, ApJS, 230, 15
Morscher M., Pattabiraman B., Rodriguez C., Rasio F. A., Umbreit S., 2015, ApJ, 800, 9
Neijssel C. J. et al., 2019, MNRAS, 490, 3740
Nitadori K., Aarseth S. J., 2012, MNRAS, 424, 545
O'Leary R. M., Rasio F. A., Fregeau J. M., Ivanova N., O'Shaughnessy R., 2006, ApJ, 637, 937
O'Leary R. M., Kocsis B., Loeb A., 2009, MNRAS, 395, 2127
O'Leary R. M., Meiron Y., Kocsis B., 2016, ApJ, 824, L12
Peters P. C., 1964, Phys. Rev., 136, 1224
Podsiadlowski P., Langer N., Poelarends A. J. T., Rappaport S., Heger A., Pfahl E., 2004, ApJ, 612, 1044
Portegies Zwart S. F., McMillan S. L. W., 2000, ApJ, 528, L17
Portegies Zwart S. F., McMillan S. L. W., 2002, ApJ, 576, 899
Portegies Zwart S. F., Yungelson L. R., 1998, A&A, 332, 173
Portegies Zwart S. F., Baumgardt H., Hut P., Makino J., McMillan S. L. W., 2004, Nature, 428, 724
Portegies Zwart S. F., McMillan S. L. W., Gieles M., 2010, ARA&A, 48, 431
Rastello S., Amaro-Seoane P., Arca-Sedda M., Capuzzo-Dolcetta R., Fragione G., Tosta e Melo I., 2019, MNRAS, 483, 1233
Renzo M., Farmer R. J., Justham S., de Mink S. E., Götberg Y., Marchant P., 2020, MNRAS, 493, 4333
Rodriguez C. L., Loeb A., 2018, ApJ, 866, L5
Rodriguez C. L., Morscher M., Pattabiraman B., Chatterjee S., Haster C.-J., Rasio F. A., 2015, Phys. Rev. Lett., 115, 051101
Rodriguez C. L., Chatterjee S., Rasio F. A., 2016, Phys. Rev. D, 93, 084029
Rodriguez C. L., Amaro-Seoane P., Chatterjee S., Kremer K., Rasio F. A., Samsing J., Ye C. S., Zevin M., 2018, Phys. Rev. D, 98, 123005
Rodriguez C. L., Zevin M., Amaro-Seoane P., Chatterjee S., Kremer K., Rasio F. A., Ye C. S., 2019, Phys. Rev. D, 100, 043027
Sadowski A., Belczynski K., Bulik T., Ivanova N., Rasio F. A., O'Shaughnessy R., 2008, ApJ, 676, 1162
Samsing J., 2018, Phys. Rev. D, 97, 103014
Samsing J., D'Orazio D. J., 2018, MNRAS, 481, 5445
Samsing J., Askar A., Giersz M., 2018, ApJ, 855, 124
Sana H. et al., 2012, Science, 337, 444
Santoliquido F., Mapelli M., Bouffanais Y., Giacobbo N., Di Carlo U. N., Rastello S., Artale M. C., Ballone A., 2020, ApJ, 898, 152
Shukirgaliyev B., Parmentier G., Berczik P., Just A., 2017, A&A, 605, A119
Sigurdsson S., Hernquist L., 1993, Nature, 364, 423
Sigurdsson S., Phinney E. S., 1995, ApJS, 99, 609
Spera M., Mapelli M., 2017, MNRAS, 470, 4739
Spera M., Mapelli M., Bressan A., 2015, MNRAS, 451, 4086
Spera M., Mapelli M., Giacobbo N., Trani A. A., Bressan A., Costa G., 2019, MNRAS, 485, 889
Spitzer L., 1987, Dynamical Evolution of Globular Clusters. Princeton Univ. Press, Princeton, NJ
Stevenson S., Berry C. P. L., Mandel I., 2017, MNRAS, 471, 2801
Stevenson S., Sampson M., Powell J., Vigna-Gómez A., Neijssel C. J., Szécsi D., Mandel I., 2019, ApJ, 882, 121
Stiefel E., 1965, J. Reine Angew. Math., 218, 204
Stone N. C., Metzger B. D., Haiman Z., 2017, MNRAS, 464, 946
Tang P. N., Eldridge J. J., Stanway E. R., Bray J. C., 2020, MNRAS, 493, L6
Tanikawa A., 2013, MNRAS, 435, 1358
Tutukov A., Yungelson L., 1973, Nauchnye Inf., 27, 70
VanLandingham J. H., Miller M. C., Hamilton D. P., Richardson D. C., 2016, ApJ, 828, 77
Voss R., Tauris T. M., 2003, MNRAS, 342, 1169
Wang L., Spurzem R., Aarseth S., Nitadori K., Berczik P., Kouwenhoven M. B. N., Naab T., 2015, MNRAS, 450, 4070
Wang L. et al., 2016, MNRAS, 458, 1450
Woosley S. E., 2017, ApJ, 836, 244
Yang Y., Bartos I., Haiman Z., Kocsis B., Márka Z., Stone N. C., Márka S., 2019, ApJ, 876, 122
Zampieri L., Roberts T. P., 2009, MNRAS, 400, 677
Zevin M., Pankow C., Rodriguez C. L., Sampson L., Chase E., Kalogera V., Rasio F. A., 2017, ApJ, 846, 82
Zevin M., Samsing J., Rodriguez C., Haster C.-J., Ramirez-Ruiz E., 2019, ApJ, 871, 91
Ziosi B. M., Mapelli M., Branchesi M., Tormen G., 2014, MNRAS, 441, 3703

This paper has been typeset from a TEX/LATEX file prepared by the author.